2D3-3

Accurate Image Expansion Method for Target Buried in Dielectric Medium Using Multi-static UWB Radar

Yoshihiro Niwa [1], Shouhei Kidera [1], Tetsuo Kirimoto [1]
[1] Graduate School of Informatics and Engineering, University of Electro-Communications, Tokyo, Japan.
Email:niwa@secure.ee.uec.ac.jp

1. Introduction

Ultra wideband (UWB) pulse radar has high dielectric permeability and range resolution, and it is thus promising for use in non-invasive imaging applications, such as non-destructive testing of pipes buried in soil or in a concrete wall, or tumor detection in early-stage breast cancer. Various imaging methods are available for near-field UWB radar systems, including synthetic aperture radar (SAR) [1], beam forming based imaging [2], time reversal focusing [3], and numerical solution of the domain integral equation with multi-dimensional optimization [4]. However, none of these methods accomplish a good performance balance between the amount of computation required and the desired accuracy or spatial resolution. As a solution to this difficulty, we have already proposed a fast and accurate imaging method [5] for targets buried in a dielectric medium based on the advanced principle of the range points migration (RPM) algorithm [6], which performs accurate surface extraction for targets in free space by using the group mapping from the range points (a set of antenna locations and observed ranges) to target surface points [5]. The method [6] first uses the boundary points of the dielectric medium and their normal vectors are accurately determined by RPM, and then the internal target points are reproduced by assessing the accumulation of potential target points by using a geometrical optics approximation. One notable feature of this method is that it enhances the imaging speed remarkably without use of a signal integration approach, and improves the accuracy of target boundary extraction to the order of 1/100 of a wavelength.

However, the RPM method [6] assumes a mono-static configuration in the observation event, and often barely reconstructs the whole of the target boundary, particularly for a dielectric medium with a random surface. This then poses a difficulty in distinguishing the exact shape of an internal target, which could be critical in applications such as discrimination of a deformed pipe in a non-destructive testing application. To enhance the imaging area of an internal target, this paper introduces a novel method using multi-static observation, where the principle of the method in [6] is extended appropriately to a single-transmitting and multiple-receiving model. This method can enhance the instantaneous aperture size, which makes it possible to obtain the reflection echo from a wider part of the target boundary. The results of numerical simulations show that the proposed method accurately expands the imaging region of the internal target compared with that obtained using the mono-static based method.

2. System Model

Figure 1 shows the system model. We assume that the target and the dielectric medium with uniform permittivity have arbitrary shapes with clear boundaries, and the relative permittivity is given as ϵ_r. The propagation speed c of a radio wave in air is a known constant. A number of omnidirectional antennas are arranged in a circle, the inner region of which completely surrounds a dielectric medium. A monocycle pulse is used as the transmitting current, with center wavelength denoted as λ. The real space in which the target and the antennas are located is defined by the parameter $\boldsymbol{r} = (x, z)$. $s(\boldsymbol{r}_\mathrm{T}, \boldsymbol{r}_\mathrm{R}, R)$ is defined as the output of the Wiener filter, where the transmitting and receiving antennas are located at $\boldsymbol{r}_\mathrm{T} = (X, Z)$ and $\boldsymbol{r}_\mathrm{R} = (X, Z)$, respectively, and $R = \mathrm{c}t/2$ is expressed using time t. The range points are defined as

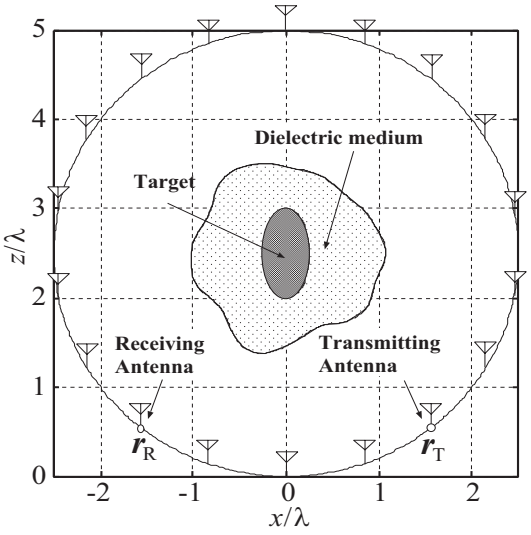

Figure 1: System model.

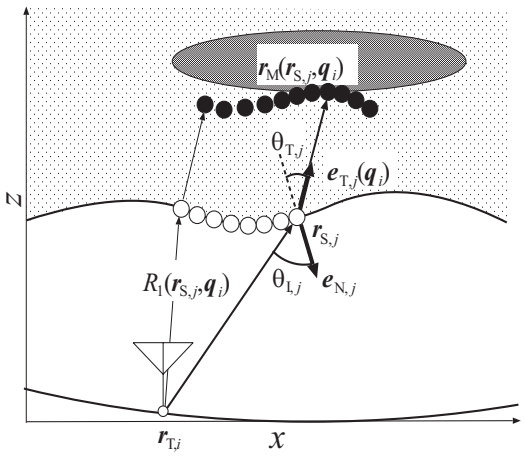

Figure 2: Spatial relationship among antennas, dielectric boundary and target points in mono-static model.

$\boldsymbol{q} = (\boldsymbol{r}_T, \boldsymbol{r}_R, R)$ and are extracted from the local maxima of $s(\boldsymbol{r}_T, \boldsymbol{r}_R, R)$, the details of this process are described in [5].

3. Conventional Method

This section briefly describes the conventional method for comparison. This method assumes mono-static observation, and first extracts the range points as $\boldsymbol{q}_{S,j} = (\boldsymbol{r}_{T,j}, \boldsymbol{r}_{R,j}, R_{S,j})$ $(j = 1, \cdots, N_S)$, where $R_{S,j}$ having a minimum R for each antenna location and $\boldsymbol{r}_{T,j} = \boldsymbol{r}_{R,j}$ holds. The dielectric boundary points $\boldsymbol{r}_{S,j} = (x_{S,j}, z_{S,j}), (j = 1, \cdots, N_S)$ are then reproduced by RPM, and are regarded as candidates for the incident points on the dielectric medium boundary. Here, all of the range points except for $\boldsymbol{q}_{S,j}$ are defined as $\boldsymbol{q}_i = (\boldsymbol{r}_{T,i}, \boldsymbol{r}_{T,i}, R_i), (i = 1, \cdots, N_M)$. As a notable feature of RPM, each normal vector $\boldsymbol{e}_{N,j}$ on the RPM boundary points $\boldsymbol{r}_{S,j}$ can be calculated without a differencing operation [6], and then, the potential target points $\boldsymbol{r}_M(\boldsymbol{r}_{S,j}, \boldsymbol{q}_i)$ corresponding to $\boldsymbol{q}_i$ can be calculated:

$$\boldsymbol{r}_M(\boldsymbol{r}_{S,j}, \boldsymbol{q}_i) = \boldsymbol{r}_{S,j} + \frac{R_i - R_1(\boldsymbol{r}_{S,j}, \boldsymbol{q}_i)}{\sqrt{\epsilon_r}} \boldsymbol{e}_{T,j}(\boldsymbol{q}_i), \tag{1}$$

where $R_1(\boldsymbol{r}_{S,j}, \boldsymbol{q}_i) = \|\boldsymbol{r}_{T,i} - \boldsymbol{r}_{S,j}\|$, $\boldsymbol{e}_{T,j}(\boldsymbol{q}_i)$ denotes the transmissive direction, which is easily calculated using $\boldsymbol{e}_{N,j}$ by Snell's law. Figure 2 shows the spatial relationship among the antenna, dielectric boundary and target boundary points assumed in mono-static observation. The method assumes that the target point exists in the set of $\boldsymbol{r}_M(\boldsymbol{r}_{S,j}, \boldsymbol{q}_i)$ and the optimal point among them is determined as:

$$\hat{\boldsymbol{r}}_M(\boldsymbol{q}_i) = \underset{\boldsymbol{r}_M(\boldsymbol{r}_{S,j}, \boldsymbol{q}_i)}{\arg\max} \sum_{l=1}^{N_M} s(\boldsymbol{q}_l) \exp\left(-\frac{\|\boldsymbol{r}_{T,i} - \boldsymbol{r}_{T,l}\|^2}{2\sigma_D^2} - \frac{(R_i - R_l)^2}{2\sigma_R^2} - \frac{\min_k \|\boldsymbol{r}_M(\boldsymbol{r}_{S,j}, \boldsymbol{q}_i) - \boldsymbol{r}_M(\boldsymbol{r}_{S,k}, \boldsymbol{q}_l)\|^2}{2\sigma_r^2} \right), \tag{2}$$

where σ_D, σ_R and σ_r are empirically determined constants. While this method provides an accurate internal target image with a lower computational cost, it has been confirmed that the reconstructible region is often insufficient to identify the exact target shape, because part of the inner target falls into shadow in some cases.

4. Proposed Method

To overcome the above difficulty, this paper introduces an image expansion scheme using the multi-static observation model. Because the imaging principle itself is similar to the conventional method, we focus on the formulation specific to the multi-static model as follows. In the multi-static observation, it is predicted that the incident points given as $\boldsymbol{r}_{SI,j}$ and the exit points given as $\boldsymbol{r}_{SE,k}$ on the dielectric

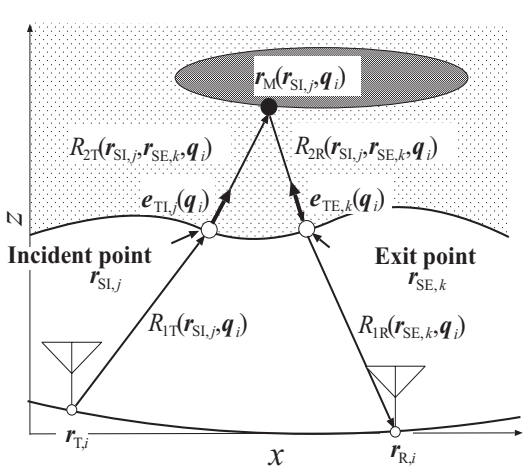

Figure 3: Possible propagation path in multi-static observation.

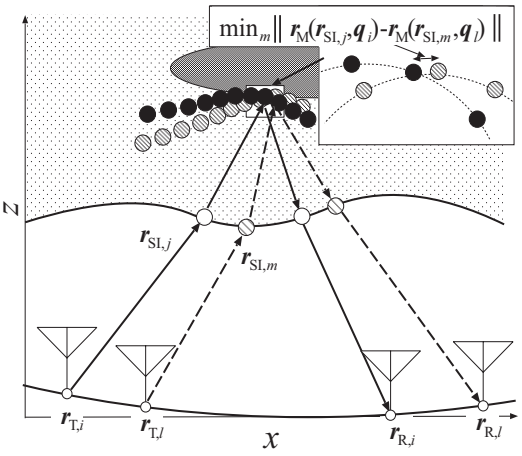

Figure 4: Spatial relationship between the two groups of the candidate points $\boldsymbol{r}_{\mathrm{M}}(\boldsymbol{r}_{\mathrm{SI},j}, \boldsymbol{q}_i)$ and $\boldsymbol{r}_{\mathrm{M}}(\boldsymbol{r}_{\mathrm{SI},m}, \boldsymbol{q}_l)$.

boundary have different locations, and thus a pairing process is needed for them in this model. Figure 3 shows the possible propagation path under multi-static observation. Using the normal vector on each dielectric point, the intersection point between the incident and exit paths can be calculated as $\boldsymbol{r}_{\mathrm{M}}(\boldsymbol{r}_{\mathrm{SI},j}, \boldsymbol{q}_i)$ shown in Fig. 3. Then, the propagation ranges in the dielectric medium given as $R_{2\mathrm{T}} = \|\boldsymbol{r}_{\mathrm{SI},j} - \boldsymbol{r}_{\mathrm{M},j}\|$ and $R_{2\mathrm{R}} = \|\boldsymbol{r}_{\mathrm{SE},k} - \boldsymbol{r}_{\mathrm{M},j}\|$ are determined as:

$$\begin{bmatrix} R_{2\mathrm{T}}(\boldsymbol{r}_{\mathrm{SI},j}, \boldsymbol{r}_{\mathrm{SE},k}, \boldsymbol{q}_i) \\ R_{2\mathrm{R}}(\boldsymbol{r}_{\mathrm{SI},j}, \boldsymbol{r}_{\mathrm{SE},k}, \boldsymbol{q}_i) \end{bmatrix} = \sqrt{\varepsilon_r} \left[\boldsymbol{e}_{\mathrm{TI},j}(\boldsymbol{q}_i), -\boldsymbol{e}_{\mathrm{TE},k}(\boldsymbol{q}_i) \right]^{-1} \left(\boldsymbol{r}_{\mathrm{SI},k} - \boldsymbol{r}_{\mathrm{SE},j} \right), \tag{3}$$

where, $\boldsymbol{e}_{\mathrm{TI},j}(\boldsymbol{q}_i)$ and $\boldsymbol{e}_{\mathrm{TE},k}(\boldsymbol{q}_i)$ denote the penetration directions from $\boldsymbol{r}_{\mathrm{SI},j}$ and $\boldsymbol{r}_{\mathrm{SE},k}$, respectively, which are determined in a similar way to the method of [6]. Using $R_{2\mathrm{T}}$ and $R_{2\mathrm{R}}$, the desired exit point as $\hat{\boldsymbol{r}}_{\mathrm{SE}}(\boldsymbol{r}_{\mathrm{SI},j}, \boldsymbol{q}_i)$ is determined as:

$$\hat{\boldsymbol{r}}_{\mathrm{SE}}(\boldsymbol{r}_{\mathrm{SI},j}, \boldsymbol{q}_i) = \underset{\boldsymbol{r}_{\mathrm{SE},k}}{\arg\min} \left| R_i - \tilde{R}(\boldsymbol{r}_{\mathrm{SI},j}, \boldsymbol{r}_{\mathrm{SE},k}, \boldsymbol{q}_i) \right|, \tag{4}$$

where $\tilde{R}(\boldsymbol{r}_{\mathrm{SI},j}, \boldsymbol{r}_{\mathrm{SE},k}, \boldsymbol{q}_i) = R_{1\mathrm{T}}(\boldsymbol{r}_{\mathrm{SI},j}, \boldsymbol{q}_i) + R_{1\mathrm{R}}(\boldsymbol{r}_{\mathrm{SE},k}, \boldsymbol{q}_i) + R_{2\mathrm{T}}(\boldsymbol{r}_{\mathrm{SI},j}, \boldsymbol{r}_{\mathrm{SE},k}, \boldsymbol{q}_i) + R_{2\mathrm{R}}(\boldsymbol{r}_{\mathrm{SI},j}, \boldsymbol{r}_{\mathrm{SE},k}, \boldsymbol{q}_i)$, $R_{1\mathrm{T}}(\boldsymbol{r}_{\mathrm{SI},j}, \boldsymbol{q}_i) = \|\boldsymbol{r}_{\mathrm{T},i} - \boldsymbol{r}_{\mathrm{SI},j}\|$ and $R_{1\mathrm{R}}(\boldsymbol{r}_{\mathrm{SE},k}, \boldsymbol{q}_i) = \|\boldsymbol{r}_{\mathrm{R},i} - \boldsymbol{r}_{\mathrm{SE},k}\|$. For each $\boldsymbol{q}_i$, the potential target points $\boldsymbol{r}_{\mathrm{M}}(\boldsymbol{r}_{\mathrm{SI},j}, \boldsymbol{q}_i)$ are calculated:

$$\boldsymbol{r}_{\mathrm{M}}(\boldsymbol{r}_{\mathrm{SI},j}, \boldsymbol{q}_i) = \boldsymbol{r}_{\mathrm{SI},j} + \frac{R_{2\mathrm{T}}(\boldsymbol{r}_{\mathrm{SI},j}, \hat{\boldsymbol{r}}_{\mathrm{SE}}(\boldsymbol{r}_{\mathrm{SI},j}, \boldsymbol{q}_i), \boldsymbol{q}_i)}{\sqrt{\epsilon_r}} \boldsymbol{e}_{\mathrm{TI},j}(\boldsymbol{q}_i). \tag{5}$$

Based on a similar approach to the method of [6], the optimum candidate for the internal target point $\hat{\boldsymbol{r}}_{\mathrm{M}}(\boldsymbol{q}_i)$ is calculated as

$$\hat{\boldsymbol{r}}_{\mathrm{M}}(\boldsymbol{q}_i) = \underset{\boldsymbol{r}_{\mathrm{M}}(\boldsymbol{r}_{\mathrm{SI},j}, \boldsymbol{q}_i)}{\arg\max} \sum_{l=1}^{N_M} s(\boldsymbol{q}_l) \exp\left(-\frac{D_{i,l}^2}{2\sigma_D^2} - \frac{(R_i - R_l)^2}{2\sigma_R^2} - \frac{\min_m \|\boldsymbol{r}_{\mathrm{M}}(\boldsymbol{r}_{\mathrm{SI},j}, \boldsymbol{q}_i) - \boldsymbol{r}_{\mathrm{M}}(\boldsymbol{r}_{\mathrm{SI},m}, \boldsymbol{q}_l)\|^2}{2\sigma_r^2} \right), \tag{6}$$

where $D_{i,l} = \min\left(\|\boldsymbol{r}_{\mathrm{T},i} - \boldsymbol{r}_{\mathrm{T},l}\| + \|\boldsymbol{r}_{\mathrm{R},i} - \boldsymbol{r}_{\mathrm{R},l}\|, \ \|\boldsymbol{r}_{\mathrm{T},i} - \boldsymbol{r}_{\mathrm{R},l}\| + \|\boldsymbol{r}_{\mathrm{R},i} - \boldsymbol{r}_{\mathrm{T},l}\| \right)$ holds. Figure 4 depicts the spatial relationship between the two groups of candidate points, $\boldsymbol{r}_{\mathrm{M}}(\boldsymbol{r}_{\mathrm{SI},j}, \boldsymbol{q}_i)$ and $\boldsymbol{r}_{\mathrm{M}}(\boldsymbol{r}_{\mathrm{SI},m}, \boldsymbol{q}_l)$. Equation (6) assesses the accumulation degree of the intersection points of the candidate curves, which is regarded as the advanced principle of the original RPM.

5. Performance Evaluation in Numerical Simulation

This section presents performance examples for each method in numerical simulation. Figures 5 and 6 show the estimated dielectric and internal target boundaries obtained by the conventional (mono-static) and proposed (multi-static) methods, respectively. A noiseless situation is assumed. For equitable

Table 1: Comparison for imaging performance in each method.

	RMSE($\times 10^{-2}\lambda$)	Reconstructible ratio[%]
Conventional(Mono-static)	6.04	60.3
Proposed(Multi-static)	1.99	97.7

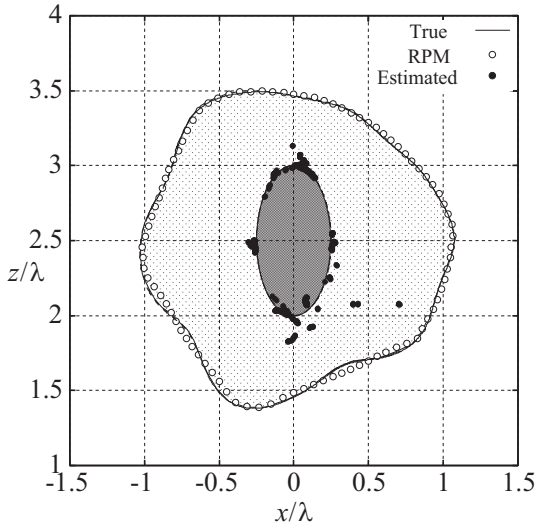

Figure 5: Dielectric and target boundary images obtained by the conventional method.

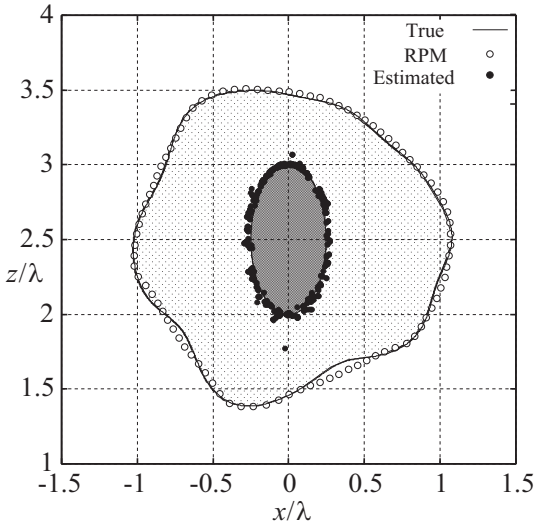

Figure 6: Dielectric and target boundary images obtained by the proposed method.

assessment in the comparison of the two methods, the number of observation points is set at 720 for the conventional model, and the number of array antennas is 36 for the proposed model, i.e. ${}_{36}\mathrm{C}_2 = 630$ independent data are usable. Here, $\sigma_D = 0.5\lambda$, $\sigma_R = 1.0\lambda$, $\sigma_r = 0.05\lambda$ are set parameters in both methods. The results here prove that while the conventional method cannot obtain the whole target boundary, our proposed method dramatically enhances the reconstructible region without significant degradation in the accuracy. For quantitative evaluation of the images obtained, the root mean square error RMSE $= \sqrt{\sum_{i=1}^{N_{\mathrm{est}}} \min \|\boldsymbol{r}_{\mathrm{true}} - \boldsymbol{r}_{\mathrm{est},i}\|^2 / N_{\mathrm{est}}}$ is defined, where r_{true} and r_{est} represent the locations of the true and estimated target points, respectively. Also, for assessment of the imaging region, the parameter $P_{\mathrm{a}} = (N'_{\mathrm{est}}/N_{\mathrm{true}}) \times 100\,[\%]$ is introduced, where N_{true} denotes the number of true target points and N'_{est} expresses the number of estimated target points that satisfy $\min_{\boldsymbol{r}_{\mathrm{true}}} \|\boldsymbol{r}_{\mathrm{true}} - \boldsymbol{r}_{\mathrm{est}}\| \leqq \epsilon_a$. Table 1 summarizes the above evaluations of both the conventional method and the proposed method, where $\epsilon_a = 0.04\lambda$ is set. This table quantitatively demonstrates that the proposed method significantly expands the imaging range with accuracy of the order of $1/100$ of the wavelength. This is because a greater instantaneous aperture size in the multi-static model makes it possible to obtain echoes from the larger part of the internal target.

References

[1] R. M. Narayanan, *et al*., *IEE Proc. Radar Sonar Navig*, vol. 151, no. 3, pp. 143-148, 2004.

[2] Martin OfHalloran, *et al*., *IEEE Trans. Biomedical Engineering*, vol. 57, no. 4, pp.830-840, April., 2010.

[3] A. Cresp, *et al*., *Proc. of EuRAD*, 2008, pp.1-4, Nov., 2008.

[4] S. D. Rajan and G. V. Frisk., *Geophysics*, vol. 54, no. 7, pp. 864-871., 1989.

[5] S. Kidera, *et al*., *IEEE Trans. Geosci. Remote Sens*., vol. 48, no. 7, pp. 1993-2004., 2010.

[6] K. Akune, *et al*., *Proc. of URSI GASS 2011*, BP-1-38, Aug., 2011.